Modelling and Simulation of a DC-excited Vernier Reluctance Machine as a Synchronous Condenser

Mkhululi Mabhula, Abraham Botes and Maarten J. Kamper
Department of Electrical and Electronic Engineering
Stellenbosch University
Stellenbosch, South Africa
mabhulamkhululi@gmail.com, 20819633@sun.ac.za, kamper@sun.ac.za

Udochukwu B. Akuru
Department of Electrical Engineering
Tshwane University of Technology
Pretoria, South Africa
AkuruUB@tut.ac.za

***Abstract*—The paper presents techniques of analysing and predicting performance for a DC-excited vernier reluctance machine as a synchronous condenser, to ensure accuracy in experimental measurements. The techniques involves finite element based models on which machine performance parameters can be calculated. The models can be used to determine the field current performance characteristics of the machine. It is shown that the presented techniques give a good performance prediction of the machine operated as a synchronous condenser when compared to experimental measured results. Furthermore, the techniques can be used in the synthesis of different types of machines when operated as synchronous condensers.**

***Index Terms*—DC-excited vernier reluctance machine, finite element method (FEM), flux linkages, synchronous condenser, two-axis modelling.**

I. Introduction

Stator-mounted double-salient wound-field machines are lately becoming an interesting machine variant due to their avoidance of expensive PMs, less copper volume mainly as a result of concentrated winding layouts, robust rotor topologies, as well as easy thermal management due to their stator-active profiles. Among these machine variants, the wound-field flux switching machine (WF-FSM) [1] and the DC Vernier reluctance machine (DC-VRM) [2] stand out due to extended operational limits and improved machine reliability in terms of brushless adjustable DC field exciters, as well as the possibility for obtaining symmetric sinusoidal flux linkage and back-electromotive force waveforms.

However, a major challenge for these machine selections is an overwhelmed stator comprising both DC field and phase windings which tend to increase and complicate the magnetic activity on the stator core, leading it into short-term saturation [2]. Besides, due to a double salient rotor structure and slotting effects of the stator and rotor magnetomotive force harmonics on the air-gap permeance, torque ripple which result in mechanical vibrations and acoustics, can be prominent [3].

Notwithstanding, the highlighted design (no need for brushes and slip rings) and performance (high torque density) benefits of these machine topologies e.g., in wind power generation, especially at industrial-scale power levels, cannot be overlooked [4]. Moreover, it is left to be seen how these non-classical synchronous machines, having robust rotor and brushless DC excitation, would fare if designed as synchronous condensers – used for reactive power compensation and voltage regulation in electrical power networks. The latter case is becoming necessary considering that high penetration of renewable energy power generation leads to reduced grid inertia and power system network instability in the long run [5].

For the authors, an attempt has been made in the past to design, implement and successfully test the WF-FSM as synchronous condensers for the first time [6], [7]. In the present study, the focus is on developing design techniques for analysing and predicting performance of a DC-VRM as a synchronous condenser to ensure accuracy in experimental measurements. To achieve this, a small-scale prototype machine is studied theoretically and experimentally for technology demonstration. The rest of the study is structured as follows: Section II is used to introduce the DC-VRM SC technology while Section III is used to described the SC operating principle; Section IV is on modelling of the SC while Section V gives results on the simulation; Section VI is on the experiments performed to test the theory, while Section VII is used to give some concluding remarks.

II. DC-VRM technology as a SC

DC-VRMs are novel type of machines which adopt stationary field winding to generate the exciting field, and their rotor have no PMs or winding, as a result, brush and slip-rings are not necessary [8]–[12]. The machines are equipped with non-overlapped single tooth concentrated coils. These machines exhibit good performance such as low joule losses, high efficiency, reduced material, and manufacturing costs, robustness rotor structure, and easy heat dissipation. Therefore, in applications requiring low cost, high reliability, and high speed these machines have been gaining more and more research attention.

With the above mentioned attributes, the DC-VRM technology is employed in this paper as SC. Shown in Fig. 1, is the double top and bottom slotted structure of the studied DC-VRM. The phase (1, 2, 3) and field (4) coil connections of the DC-VRM are shown in a 12-stator-pole with 10-rotor-pole

978-0-7381-1236-7/21/$31.00 ©2021 IEEE

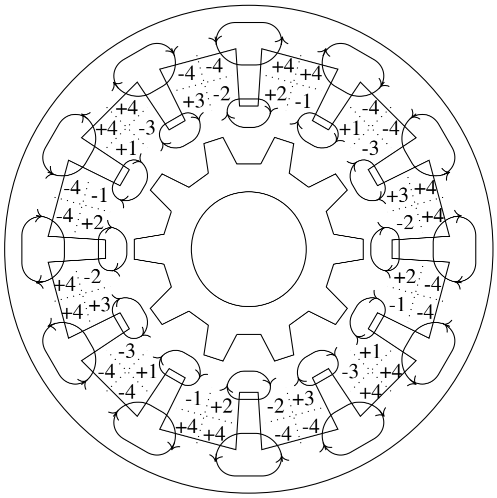

Fig. 1. DC-VRM topology, connection of phase and field coils in 12-stator-pole with 10-rotor-pole and 12/10 stator/rotor slots.

(12s10r) arrangement. Both four coils per phase and twelve field coils are connected in series.

III. SC OPERATING PRINCIPLE

The SC operates at no-load angles ($\delta \approx 0°$) with controlled field excitation as illustrated in Fig. 2. This is achieved by reducing the electrical load on the SC such that the active power to/from the SC is zero i.e. power factor becomes zero as shown in Fig. 2(a). As the field excitation increases at no-load Fig. 2(b), the induced voltage E increases, and the SC current becomes higher leading the terminal voltage V. Since the power factor remains zero i.e. $\alpha \approx 90°$, there is no active power transferred, but a high and controllable level of reactive power. In Fig. 2(b), the field current (leading the voltage) increases above rated to supply reactive power i.e. over-excited. Also, the field current can be reduced below rated to absorb reactive power i.e. under-excited. Thus the machine will absorb (under-excited) and generate (over-excited) reactive power to the supply system of fixed voltage as illustrated in the so called V-curve of Fig. 3.

IV. SC MODELING

The k^{th} phase terminal voltage of a SC is given by Faraday's Law and copper loss components represented in the m-phase reference frame. In general, the electromagnetic behavior of the voltage is described as [13]

$$v_k = i_k R_k + \frac{d}{dt}\lambda_k, \quad k = 1, 2, \ldots, m \tag{1}$$

where $m = 3$ is the number of phases and R_k, i_k, and λ_k are the k^{th} phase resistance, current, and flux linkage (including the end-winding effects) respectively. At steady-state, (1) is simplified as

$$v_k = i_k R_k + \omega\lambda_k, \quad k = 1, 2, \ldots, m \tag{2}$$

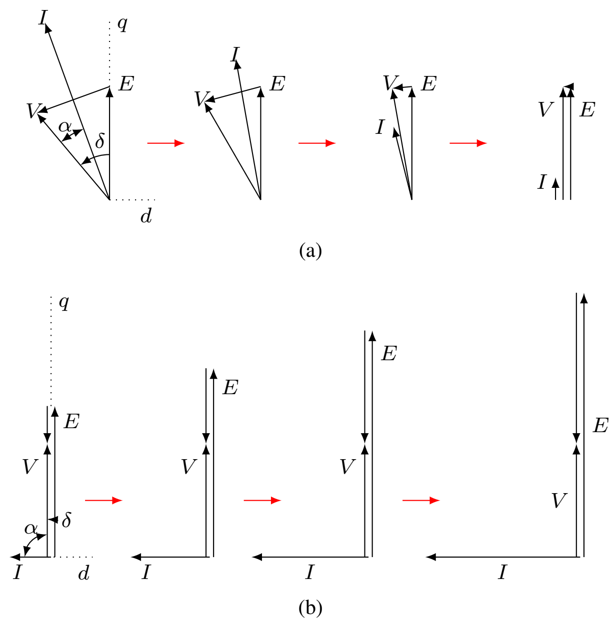

Fig. 2. SC principle of operation showing successive (a) decrease in load angle and (b) increase in field current at no-load i.e. $\delta = \alpha = 0°$.

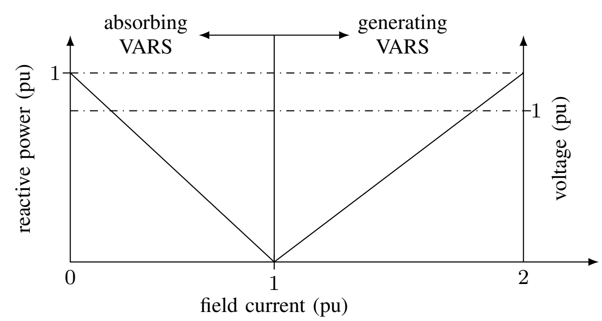

Fig. 3. Example of a V-curve for a synchronous condenser.

where ω is the electrical angular frequency. Furthermore, in a balanced phase voltage supply system, the k^{th} phase voltage of (1) is given by

$$v_k = -V \sin[\theta + \delta - (k-1)\frac{2\pi}{m}], \quad k = 1, 2, \ldots, m \tag{3}$$

where θ, and δ are the electrical rotor position, and voltage shift angles respectively and V is the supply voltage magnitude. Utilizing Park's transformation [14], i.e. direct d and quadrature q axes rotating at ω fixed on the rotor, the dq-axes voltages of (3) also described in (2) are expressed as

$$\begin{aligned} V_d &= \{I_d\}R_k - \omega(\{I_q\}L_e + \{\Lambda_q\}) \\ V_q &= \{I_q\}R_k + \omega(\{I_d\}L_e + \{\Lambda_d\}), \end{aligned} \tag{4}$$

where L_e is the analytical calculated end-winding inductance as from [15]. Thus, the line terminal voltage can be calculated as

$$V_L = \sqrt{1.5(V_d^2 + V_q^2)}. \tag{5}$$

In (4), the parameters in bracelets, $\{I_d, I_q\}$ and $\{\Lambda_d, \Lambda_q\}$, are the solved dq-axes currents and flux linkages of (2),

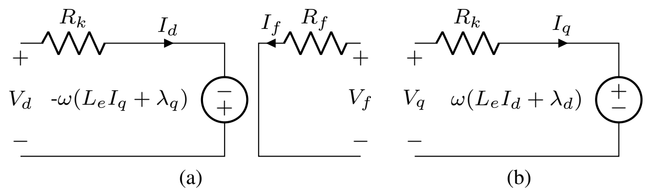

Fig. 4. SC (a) d and (b) q axes equivalent circuit diagram.

respectively from the defined voltage supply system of (3) calculated by utilizing Park's transformation as

$$
\begin{aligned}
I_d &= \frac{2}{m}\sum_{k=1}^{m} i_k \cos[\theta-(k-1)\frac{2\pi}{m}] \\
I_q &= -\frac{2}{m}\sum_{k=1}^{m} i_k \sin[\theta-(k-1)\frac{2\pi}{m}],
\end{aligned}
\tag{6}
$$

and

$$
\begin{aligned}
\Lambda_d &= \frac{2}{m}\sum_{k=1}^{m} \lambda_k \cos[\theta-(k-1)\frac{2\pi}{m}]k \\
\Lambda_q &= -\frac{2}{m}\sum_{k=1}^{m} \lambda_k \sin[\theta-(k-1)\frac{2\pi}{m}]i_k.
\end{aligned}
\tag{7}
$$

Figure 4 shows the dq-axis equivalent circuit diagram resulting from (4). In Fig. 4, the field voltage is calculated from the field current I_f and equivalent resistance R_f as

$$V_f = I_f R_f. \tag{8}$$

The relative positions between the dq-axis voltage, current and flux linkages of (4)-(7) are shown in Fig. 5. It can be observed from Fig. 5 that given $\gamma = 90°$ at a fixed voltage magnitude i.e. V, all the currents and flux linkages depend on the voltage/load angle δ. Consequently, δ is used to facilitate loading on the SC. Henceforth, following Fig. 5 the dq-axis voltages (in the direction of phase-1 magnetic axis when phase-1 voltage peaks) are defined by

$$V_d = V\sin(\delta), \quad V_q = V\cos(\delta). \tag{9}$$

Furthermore, the flux linkages of (7) can be expressed in terms of the effective reactances as [16]

$$\Lambda_d = (I_d X_d + I_f X_f)/\omega, \quad \Lambda_q = I_q X_q/\omega \tag{10}$$

where X_d, X_q and X_f are reactances arising from d-, q- and f-axes currents respectively. The phase input active (P) and reactive (Q) powers are calculated from

$$P = 1.5(V_d I_d + V_q I_q), \quad Q = 1.5(V_q I_d - V_d I_q), \tag{11}$$

from which the apparent power is calculated as

$$S = \sqrt{P^2 + Q^2}. \tag{12}$$

The total losses are given by

$$P_l = P_{cu} + P_r \tag{13}$$

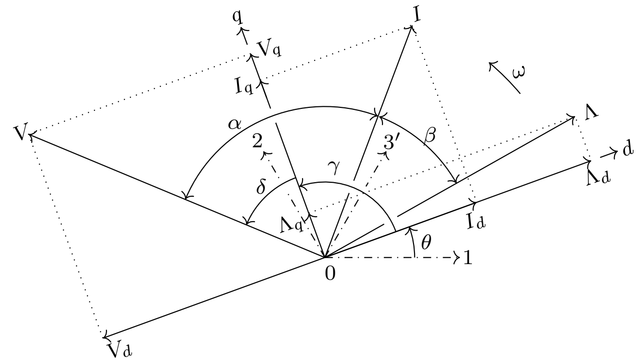

Fig. 5. SC phasor diagram as motor showing 123-phases and dq-axes relative positions of voltage, current and flux linkage.

where P_{cu} and P_r are copper and rotational losses respectively. The copper losses are calculated from

$$P_{cu} = P_s + P_f = 1.5R_k(I_d^2 + I_q^2) + R_f I_f^2. \tag{14}$$

The rotational losses are given as the sum of core and windage-and-friction losses given by

$$P_r = P_c + P_{wf}. \tag{15}$$

In (15), the core losses are a sum of stator and rotor core losses calculated using FEM packages [17]. The windage-and-friction losses are approximated as in [18]. Lastly, it is also easy to calculate the electromagnetic torque from (6) and (7) as [8]

$$T = 1.5N_r(\Lambda_d I_q - \Lambda_q I_d). \tag{16}$$

V. SC Simulation Strategy

Two-dimensional transient Ansys-Maxwell [19] and static SEMFEM [17] FEM are used in the performance calculation of the SC. Ansys-Maxwell and SEMFEM are commercial and in-house FEM software packages respectively. Since SEFMEM is a magneto-static FEM, the performance comparison is done at steady-state.

The rated field current $I_{f(\text{rated})}$ is given when $Q = 0$ VAR, hence the maximum allowable field current $I_{f(\max)}$ is when $I_f = 2I_{f(\text{rated})}$. Following the latter, the field current should be in the range given by

$$0 \leqslant I_f \leqslant I_{f(\max)}. \tag{17}$$

Figure 6 shows the flow diagram utilizing the two mentioned FEMs. In Fig. 6, j is the flow diagram iterative process counter which is initialised (i.e. $j = 1$) at the beginning of the process. For a 3-phase system ($m = 3$), to calculate the supply system voltage of (3) at the SC terminals, the load angle δ defined in Fig. 5 at no-load is set 0°. Hence, using (9), $V_d = 0$ and $V_q = V$ at an angular speed defined by ω. Both phase and field resistances are generally calculated from [18]

$$R = \frac{\rho W \ell}{A} \tag{18}$$

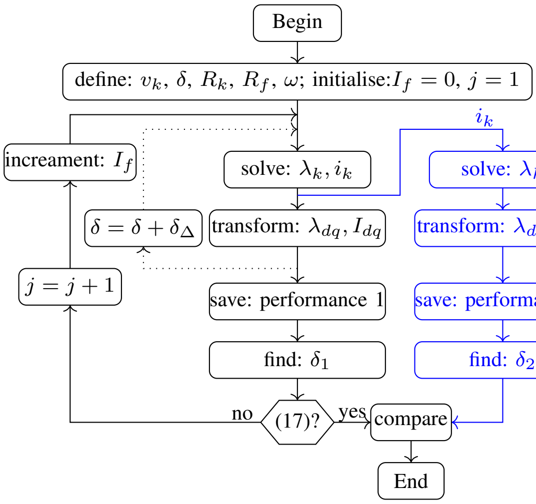

Fig. 6. Flow diagram for solving for currents and flux linkages in performance calculation.

TABLE I. DC-VRM dimensional and winding parameters.

parameters	value	parameter	value
stator outer diameter	700.0 mm	rotor inner diameter	250 mm
stator inner diameter	154.9 mm	rotor slots	10
stator slots	12	stack length	109.6 mm
stator winding turns	69	rotor winding turns	95

where the winding parameters ρ, W, ℓ and A are material resistivity, turns per phase, total length and conductor cross-section area respectively. Following Fig. 6, given v_k, δ, R_k, R_f, ω and I_f the phase currents i_k and flux linkages λ_k are solved using Ansys-Maxwell and at steady-state transformed to dq-axis using (6) and (7) respectively. Following the latter, the performance of the SC is calculated according to (11)-(16) (performance 1 in Fig. 6). From Fig. 6, the solved dq-axis currents in Ansys-Maxwell are also used in SEMFEM to solve for dq-axis flux linkages λ_d, λ_q which are in turn used to also calculated the SC performance according to (11)-(16) (performance 2 in Fig. 6).

It is important to state that SCs draws a small amount of active power from the system to supply losses as of (13). In this paper, a technique used in [20] of performance maps is utilised to find the load angle to compensate for the small drawn active power by the SC. Thus in Fig. 6, after calculating saving the performances at different load angles, the performances are mapped in both Ansys-Maxwell and SEMFEM for find the load angles δ_1 and δ_2 in Fig. 6, respectively. It is these load angles which are then used for the actual performance of the SC.

Figure 7 shows Ansys-Maxwell and SEMEFEM 2D axial view DC-VRM models with winding configuration as shown in Fig. 1. Table I gives the SC parameters. A M400-50A BH curve lamination material is used to take into account the saturation effects in the SC. Figure 8 shows the open-circuit voltage (i.e. induced-voltage, E) of the DC-VRM simulate in Ansys-Maxwell and SEMFEM. Figure 9 shows the 400 V/50

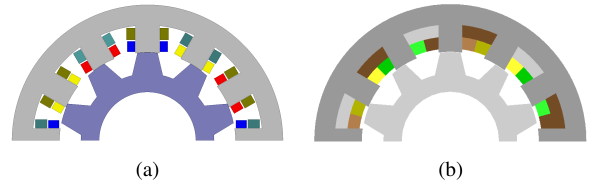

Fig. 7. DC-VRM (a) Ansys-Maxwell and (b) SEMFEM 2D axial view models.

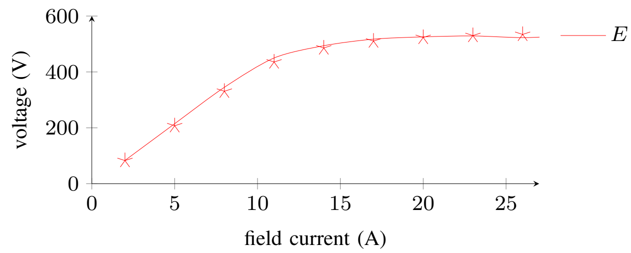

Fig. 8. DC-VRM line open-circuit voltage versus field current. Continuous lines-SEMFEM, only markers-Ansys-Maxwell, blue mark-rated operating point.

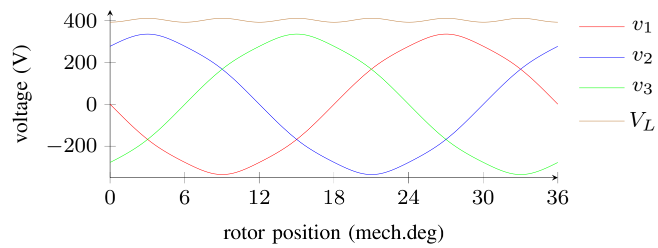

Fig. 9. SC supply system (grid) phase voltages versus rotor position.

Hz phase voltages of (3) and line voltages of (5) versus rotor position used as the SC supply. With phase voltages Fig. 9 as the supply and field current varied, the performance of the SC can be determined. Figures 10-13 shows the SC performance comparison at an operating speed of 300 rpm of Ansys-Maxwell and SEMFFEM when the field current is in range defined by (17) ($0 \leqslant I_f \leqslant 18$) A with $\delta = 0°$. Figure 10 shows the dq-axis voltages of (4) versus field current calculated in both FEM software packages at no-load. The absolute dq-axis and field current values solved from Ansys-Maxwell and also used in SEMFEM are shown in Fig. 11. The resulting dq-axis flux linkages from both software packages are shown in Fig. 12. The powers of the SC calculated from (11) are shown in Fig. 13. As expected from the above discussed results according to Section III when $\delta = 0°$, $V_d = I_q = \lambda_q = P \approx 0$.

A good agreement between the two software packages is shown in all the performance characteristics of the SC in Figs. 10-13. However, it is important to state that since SEMFEM is a static package, it is well suited in design optimization of the SC.

In addition, Fig. 14 shows the effective dq-axis reactances calculated using (10) from the results in Figs. 11 and 12. From Fig. 14, both the d and q axes reactances are not affected by

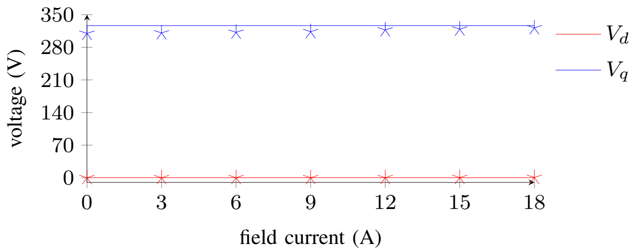

Fig. 10. SC calculated dq-axes voltages versus field current. Continuous lines-SEMFEM, only markers-Ansys-Maxwell.

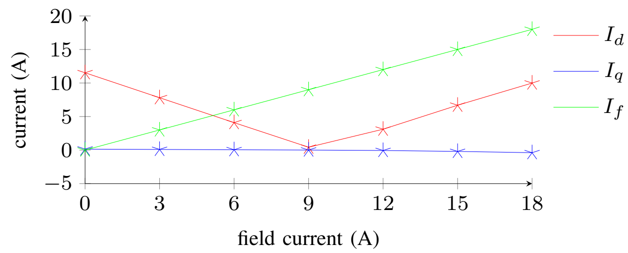

Fig. 11. SC solved dq-axes currents versus field current. Continuous lines-SEMFEM, only markers-Ansys-Maxwell.

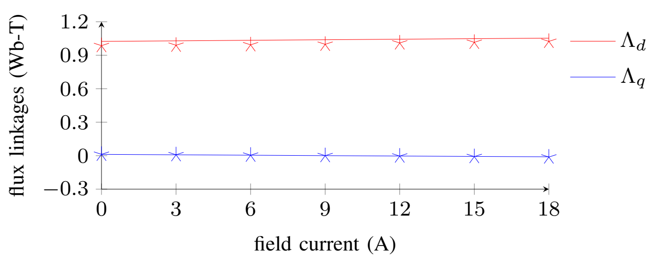

Fig. 12. SC solved dq-axes flux linkages versus field current. Continuous lines-SEMFEM, only markers-Ansys-Maxwell.

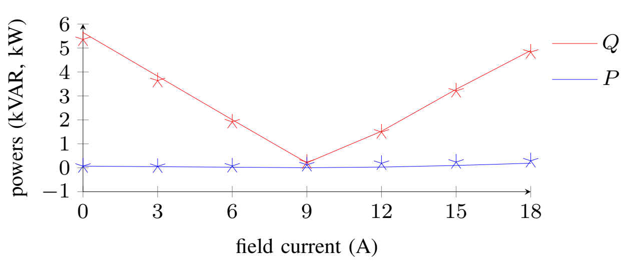

Fig. 13. SC calculated powers versus field current. Continuous lines-SEMFEM, only markers-Ansys-Maxwell.

saturation when the machine is absorbing reactive power i.e. Fig. 13 when $I_f \leqslant 9$ A with reference to Fig. 3. However, when the SC is generating reactive power i.e. Fig. 13 when $I_f \geqslant 9$ A, both d and q axes reactances of the SC are affected by saturation. As shown in Fig. 14 the reactances decrease as the field increases when $I_f \geqslant 9$ A.

VI. Experimental equipment and test results

A prototype of a DC-VRM to be tested as a SC with parameters given in Table I was built and tested. The machine is designed to operate at 300 rpm, with a 400 V, 50 Hz supply

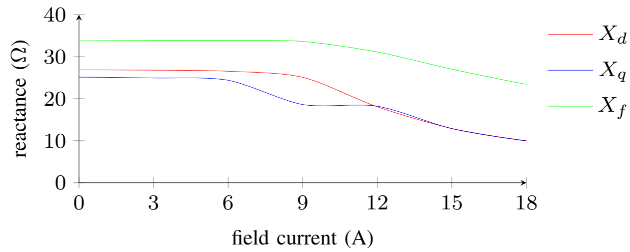

Fig. 14. SC calculated reactance versus field current. Continuous lines-SEMFEM, only markers-Ansys-Maxwell.

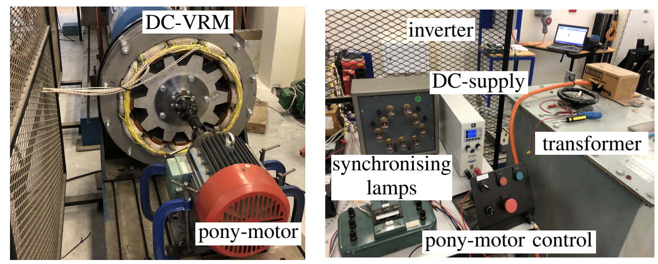

Fig. 15. DC-VRM laboratory experimental setup.

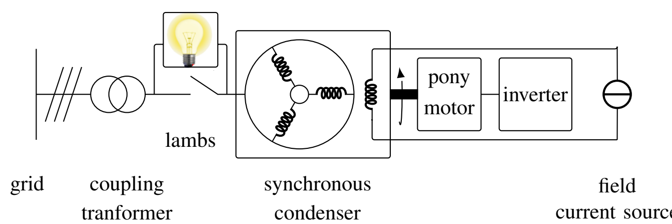

Fig. 16. Laboratory setup block diagram.

system. However, due to mechanical issues in construction the machine was derated to 160 V in this experimental study. It is important to state that, the machine under study here was initially design as a generator [9], however, implemented as SC in this paper. Figure 15 shows the experimental setup of the DC-VRM to be tested as a SC. Figure 16 shows the experimental setup block diagram. A pony motor speed controlled by an inverter is attached to the DC-VRM to facilitate grid synchronism with the help of lamps. A grid connected variable voltage transformer is used as the SC supply system. The DC power supply provides the necessary field current.

Now knowing the supply system voltage, the total losses of (13) can be mapped with the load angles in simulation [20]. Thus with the total losses of the machine, the load angle can be read from the maps which can be used in both Ansys-Maxwell and SEMFEM for the SC performance prediction to the measured results. Figures 17 and 18 shows a good agreement between measured and simulated results. Thus these results validates the SC simulation strategy presented in Section V.

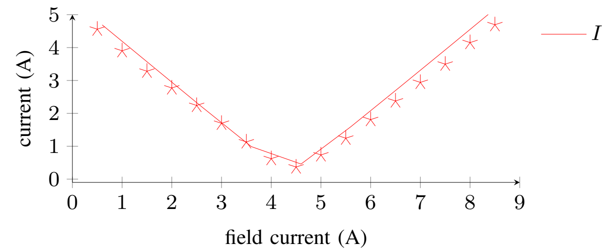

Fig. 17. DC-VRM current versus field current. Continuous lines-simulated, only markers-measured.

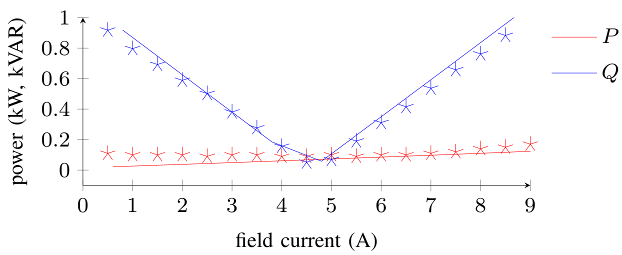

Fig. 18. DC-VRM powers versus field current. Continuous lines-simulated, only markers-measured.

VII. Conclusions

In this paper, simulation strategies of analysing a DC-VRM as a synchronous condenser to ensure accuracy in experimental measurements are presented. The simulation strategies are successfully implemented on the DC-VRM as a SC to predict the machine performance in operations of absorbing and generating reactive power to the grid. With validation using experimental results, it is possible to predict accurately the practical performance of the DC-VRM as a SC using the simulation strategies. To this end, the proposed analysis technique can be used in the synthesis of different types of machines designed for synchronous condensers.

In addition to the above conclusions, it is important to recommend that using bolts (see Fig. 15) to stack the machine laminations of such a structure comes with mechanical challenges when the machine is not constructed in a proper frame. If the structure is not symmetric, there is an unbalanced magnetic pull as the field current increases hence, the magnetic field pulls the rotor to the closest pole causing it to lock or knock on the stator.

Lastly, among other machine technologies, the DC-VRM can be utilised as a SC to provide stability on the South African electricity network, with growing renewable energy penetration. This is because of the mechanical (robust rotor structure) and electrical (brushless DC field excitation system) benefits of the machine technology.

Acknowledgment

The authors would like to thank the Centre for Renewable and Sustainable Energy Studies (CRSES) at Stellenbosch University for the financial support of this study. The authors wish to acknowledge Kenan Cloete, Andrew Loubser and the staff of the Electrical Workshop of Stellenbosch University for the assistance in machine construction and laboratory experimental tests.

References

[1] A. Zulu, B. C. Mecrow, and M. Armstrong, "A wound-field three-phase flux-switching synchronous motor with all excitation sources on the stator," *IEEE Transactions on Industry Applications*, vol. 46, no. 6, pp. 2363–2371, 2010.

[2] X. Liu and Z. Q. Zhu, "Electromagnetic performance of novel variable flux reluctance machines with dc-field coil in stator," *IEEE Transactions on Magnetics*, vol. 49, no. 6, pp. 3020–3028, 2013.

[3] M. Lin, R. Qu, J. Li, S. Jia, and Y. Lu, "Torque ripple reduction techniques for stator dc winding excited vernier reluctance machines," in *2016 IEEE Energy Conversion Congress and Exposition (ECCE)*, 2016, pp. 1–8.

[4] U. B. Akuru and M. J. Kamper, "Intriguing behavioral characteristics of rare-earth-free flux switching wind generators at small- and large-scale power levels," *IEEE Transactions on Industry Applications*, vol. 54, no. 6, pp. 5772–5782, 2018.

[5] C. Szabo. Synchronous condensers: An old tool rediscovered to address new grid challenges, Power Engineering international. Accessed: 2019-09-15. [Online]. Available: https://www.powerengineeringint.com/news/an-old-tool-rediscovered-to-address-new-grid-challenges/

[6] U. B. Akuru and M. J. Kamper, "A modest attempt on the electromagnetic design and performance prediction of turbo wound-field flux switching synchronous condensers," in *2019 IEEE Energy Conversion Congress and Exposition (ECCE)*, 2019, pp. 1782–1789.

[7] C. Africa, U. B. Akuru, and M. J. Kamper, "Bringing back the synchronous compensator for the south africa power network—simulation and compensator technology," in *2019 Southern African Universities Power Engineering Conference/Robotics and Mechatronics/Pattern Recognition Association of South Africa (SAUPEC/RobMech/PRASA)*, 2019, pp. 648–654.

[8] M. Mabhula, U. B. Akuru, and M. J. Kamper, "Cross-coupling inductance parameter estimation for more accurate performance evaluation of wound-field flux modulation machines," *Electronics*, vol. 9, no. 11, August 2020.

[9] U. B. Akuru, M. J. Kamper, and M. Mabhula, "Optimisation and design performance of a small-scale dc vernier reluctance machine for direct-drive wind generator drives," in *2020 IEEE Energy Conversion Congress and Exposition (ECCE)*, 2020, pp. 2965–2970.

[10] S. Jia, R. Qu, J. Li, and D. Li, "Principles of stator dc winding excited vernier reluctance machines," *IEEE Transactions on Energy Conversion*, vol. 31, no. 3, pp. 935–946, 2016.

[11] X. Zhu, C. H. T. Lee, C. C. Chan, L. Xu, and W. Zhao, "Overview of flux-modulation machines based on flux-modulation principle: Topology, theory, and development prospects," *IEEE Transactions on Transportation Electrification*, vol. 6, no. 2, pp. 612–624, 2020.

[12] X. Y. Sun, Z. Q. Zhu, and F. R. Wei, "Voltage pulsation induced in dc field winding of different hybrid excitation switched flux machines," in *2020 IEEE Energy Conversion Congress and Exposition (ECCE)*, 2020, pp. 4681–4688.

[13] T. A. Lipo, *Analysis of synchronous machines*. CRC Press, June 2012.

[14] A. A. Rockhill and T. A. Lipo, "A generalized transformation methodology for polyphase electric machines and networks," in *2015 IEEE International Electric Machines Drives Conference (IEMDC)*, 2015, pp. 27–34.

[15] J. H. J. Potgieter and M. J. Kamper, "Evaluation of calculation methods and the effect of end-winding inductance on the performance of non overlap winding pm machines," in *2012 XXth International Conference on Electrical Machines*, 2012, pp. 243–249.

[16] J. Pyrhoenen, T. Jokinen, and V. Hrabovcova, *Design of rotating electrical machines*. Wiley, November 2013.

[17] S. Gerber, *SEMFEM User's Manual*, Stellenbosch University, May 2014.

[18] M. G. Say, *Alternating current machines*, 5th ed. Longman Scientific and Technology, 1992.

[19] Ansys, Inc, "Ansys Maxwell: Low frequency electromagnetic field simulation," Accessed: 2020-06-05. [Online]. Available: https://www.ansys.com/products/electronics/ansys-maxwell

[20] M. Mabhula and M. J. Kamper, "Model parameter and performance calculation of cylindrical wound-rotor synchronous motors," *IEEE Transactions on Energy Conversion*, pp. 1–1, 2020.